

essential in the pairing of CFs and the formation of the  $\nu = 5/2$  FQH state at low temperature.

Our NMR experiments have demonstrated maximal spin polarization for the  $\nu = 5/2$  FQH state over a wide range of electron densities. These measurements are consistent with the nonabelian Pfaffian state (5) and the anti-Pfaffian state (9, 10), while unambiguously ruling out the unpolarized (331) state (11), which had been the most likely abelian contender (13). However, the exciting prospect of topologically protected quantum operations using the  $\nu = 5/2$  FQH state awaits a direct experimental demonstration of its nonabelian nature.

#### References and Notes

1. D. C. Tsui, H. L. Stormer, A. C. Gossard, *Phys. Rev. Lett.* **48**, 1559 (1982).
2. R. B. Laughlin, *Phys. Rev. Lett.* **50**, 1395 (1983).
3. J. K. Jain, *Phys. Rev. Lett.* **63**, 199 (1989).
4. R. L. Willett *et al.*, *Phys. Rev. Lett.* **59**, 1776 (1987).
5. G. Moore, N. Read, *Nucl. Phys. B* **360**, 362 (1991).
6. M. Greiter, X. G. Wen, F. Wilczek, *Nucl. Phys. B* **374**, 567 (1992).
7. C. Nayak, F. Wilczek, *Nucl. Phys. B* **479**, 529 (1996).

8. C. Nayak, S. H. Simon, A. Stern, M. Freedman, S. Das Sarma, *Rev. Mod. Phys.* **80**, 1083 (2008).
9. M. Levin, B. I. Halperin, B. Rosenow, *Phys. Rev. Lett.* **99**, 236806 (2007).
10. S.-S. Lee, S. Ryu, C. Nayak, M. P. A. Fisher, *Phys. Rev. Lett.* **99**, 236807 (2007).
11. B. Halperin, *Helv. Phys. Acta* **56**, 75 (1983).
12. M. Dolev, M. Heiblum, V. Umansky, A. Stern, D. Mahalu, *Nature* **452**, 829 (2008).
13. I. P. Radu *et al.*, *Science* **320**, 899 (2008).
14. R. L. Willett, L. N. Pfeiffer, K. W. West, *Proc. Natl. Acad. Sci. U.S.A.* **106**, 8853 (2009).
15. V. Venkatachalam, A. Yacoby, L. Pfeiffer, K. West, *Nature* **469**, 185 (2011).
16. A. Bid *et al.*, *Nature* **466**, 585 (2010).
17. R. Morf, *Phys. Rev. Lett.* **80**, 1505 (1998).
18. I. Dimov, B. I. Halperin, C. Nayak, *Phys. Rev. Lett.* **100**, 126804 (2008).
19. A. E. Feiguin, E. Rezayi, K. Yang, C. Nayak, S. Das Sarma, *Phys. Rev. B* **79**, 115322 (2009).
20. G. Gamez, K. Muraki,  $\nu=5/2$  fractional quantum Hall state in low-mobility electron systems: Different roles of disorder; available at <http://arxiv.org/abs/1101.5856> (2011).
21. W. Desrat *et al.*, *Phys. Rev. Lett.* **88**, 256807 (2002).
22. N. Kumada, K. Muraki, Y. Hirayama, *Phys. Rev. Lett.* **99**, 076805 (2007).
23. J. H. Smet *et al.*, *Nature* **415**, 281 (2002).
24. Materials and methods are available as supporting material on Science Online.

25. X. G. Wen, *Phys. Rev. Lett.* **66**, 802 (1991).
26. M. Stern *et al.*, *Phys. Rev. Lett.* **105**, 096801 (2010).
27. T. D. Rhone *et al.*, *Phys. Rev. Lett.* **106**, 196805 (2011).
28. I. V. Kukushkin, K. von Klitzing, K. Eberl, *Phys. Rev. Lett.* **82**, 3665 (1999).
29. F. D. M. Haldane, *Phys. Rev. Lett.* **51**, 605 (1983).
30. V. W. Scarola, K. Park, J. K. Jain, *Nature* **406**, 863 (2000).
31. N. Read, D. Green, *Phys. Rev. B* **61**, 10267 (2000).
32. N. Freytag, M. Horvatic, C. Berthier, M. Shayegan, L. P. Lévy, *Phys. Rev. Lett.* **89**, 246804 (2002).

**Author contributions:** L.T. performed all the RD-NMR and transport measurements presented in this paper. G.G. performed transport measurements to optimize the samples. N.K. advised on the RD-NMR measurements. K.M. grew heterostructures and fabricated samples. L.T. and K.M. analyzed the data and wrote the paper.

#### Supporting Online Material

[www.sciencemag.org/cgi/content/full/science.1216697/DC1](http://www.sciencemag.org/cgi/content/full/science.1216697/DC1)  
Materials and Methods  
Supplementary Text  
Figs. S1 and S2  
References (33–45)

2 August 2011; accepted 19 January 2012  
Published online 26 January 2012;  
10.1126/science.1216697

# A Logic-Gated Nanorobot for Targeted Transport of Molecular Payloads

Shawn M. Douglas,\* Ido Bachelet,\* George M. Church†

We describe an autonomous DNA nanorobot capable of transporting molecular payloads to cells, sensing cell surface inputs for conditional, triggered activation, and reconfiguring its structure for payload delivery. The device can be loaded with a variety of materials in a highly organized fashion and is controlled by an aptamer-encoded logic gate, enabling it to respond to a wide array of cues. We implemented several different logical AND gates and demonstrate their efficacy in selective regulation of nanorobot function. As a proof of principle, nanorobots loaded with combinations of antibody fragments were used in two different types of **cell-signaling stimulation in tissue culture**. Our prototype could inspire new designs with different selectivities and biologically active payloads for cell-targeting tasks.

The DNA origami method (1), in which a multiple-kilobase single-stranded “scaffold” is folded into a custom shape by interaction with hundreds of oligonucleotide “staple” strands, has proved to be extremely versatile for creating custom two- and three-dimensional assemblies (2–4) that can template precise arrangement of diverse components (5–7). DNA can also be used to construct devices that perform robotic tasks such as sensing, computation, and actuation (8–11). Recently, a three-dimensional DNA origami box integrating both structural and computational components was described (12).

Inspired by these advances, we sought to design a robotic DNA device capable of selectively interfacing with cells to deliver signaling molecules to cell surfaces.

Using **cadnano**, a computer-aided design tool for DNA origami (13), we created a nanorobot in the form of a hexagonal barrel with dimensions of  $35 \text{ nm} \times 35 \text{ nm} \times 45 \text{ nm}$ . The barrel consists of two domains that are covalently attached in the rear by single-stranded scaffold hinges, and can be noncovalently fastened in the front by staples modified with DNA aptamer-based locks (Fig. 1A). Initial self-assembly proceeds in a one-pot reaction in which 196 oligonucleotide staple strands direct a 7308-base filamentous phage-derived scaffold strand into its target shape during a thermal-annealing ramp of rapid heating followed by slow cooling (14).

A clasp system based on DNA locks and DNA keys was previously used to control the

opening of the lid on a DNA box (12). To operate our device in response to proteins, we designed a DNA aptamer-based lock mechanism that opens in response to binding antigen keys (Fig. 1, B and C). Our lock system was inspired by aptamer beacons (15) and structure-switching aptamers (16), which typically undergo target-induced switching between an aptamer-complement duplex and an aptamer-target complex. We incorporated aptamer-complement duplexes on the left and right sides of the front of the barrel, such that the aptamer strands are attached to one domain and partially complementary strands are attached to the other domain. When both aptamers recognize their targets, the lock duplexes dissociate, and the nanorobot—acting as an entropic spring—undergoes a drastic reconfiguration to expose its previously sequestered surfaces. We found that shorter duplexes gave better sensitivity and faster activation rates, but at a cost of increased spontaneous activation (see text S2). We chose a lock duplex length of 23 base pairs (bp) for subsequent experiments because it displayed similar sensitivity to a shorter 16-bp duplex (activation at 10 pM) without the unacceptable loss in sensitivity observed for longer duplexes (30, 37, and 44 bp required 1 nM).

Payloads that were premodified by covalent attachment to the 5' end of a 15-base single-stranded DNA oligonucleotide linker were loaded inside the nanorobot. To enable multivalent interaction with surface receptors for potent cell stimulation (17), we aimed to load at least two payload molecules per robot. Twelve payload attachment sites were arranged in an inward-facing ring in the middle of the barrel (Fig. 1, A and C) to enable different payload orientations and spacings. The sites are staple strands with 3' extensions

Wyss Institute for Biologically Inspired Engineering and Department of Genetics, Harvard Medical School, Boston, MA 02115, USA.

\*These authors contributed equally to this work.

†To whom correspondence should be addressed. E-mail: <http://arep.med.harvard.edu/gmc/email.html>

that are complementary to a linker sequence attached to the intended cargo (Fig. 1D). After nanorobot folding and purification, cargo loading was carried out by adding linker-modified payload in molar excess to attachment sites and incubating at room temperature for 12 hours. Two types of cargo were loaded: 5-nm gold nanoparticles covalently attached to 5'-thiol-modified linkers (18), and various Fab' antibody fragments that were covalently attached to 5'-amine-modified linkers using a HyNic/4FB coupling kit (Solulink, San Diego, California). We used negative-stain transmission electron microscopy (TEM) to analyze the device in closed and open states, with and without cargo (Fig. 1F). We observed by manual counting that on average four attachment sites were populated when loading gold nanoparticles, and three sites were populated when loading antibody fragments (fig. S11).

One obstacle to overcome in constructing a "spring-loaded" device was to ensure assembly to high yield in its closed state. Like hands that set a mousetrap, two "guide" staples were in-

corporated adjacent to the lock sites that span the top and bottom domains of the device (Fig. 1E). The guide staples include 8-base toehold overhangs and could be removed after folding and purification steps by adding a 10:1 excess of fully complementary strands to the mixture (19). We observed that folding with the aid of guide staples increased the yield of closed robots from 48% to 97.5%, as assessed by manual counting of nanorobots images by TEM (fig. S17).

To examine nanorobot function, we selected a payload such that robot activation would be coupled to labeling of an activating cell (Fig. 2A). Robots loaded with fluorescently labeled antibody fragments against human leukocyte antigen (HLA)-A/B/C were mixed with different cell types expressing human HLA-A/B/C and various "key" combinations (described below) and were analyzed by flow cytometry. In the absence of the correct combination of keys, the robot remained inactive. In the inactive state, the sequestered antibody fragments were not able to bind the cell surface, resulting in a baseline fluorescence sig-

nal. However, when the robot encountered the proper combination of antigen keys, it was freed to open and bind to the cell surface via its antibody payload, causing an increase in fluorescence. We used key-neutralizing antibodies in competitive inhibition control experiments to verify that nanorobots were not activated by a non-ligand-based mechanism (fig. S25).

The robot could be programmed to activate in response to a single type of key by using the same aptamer sequence in both lock sites. Alternatively, different aptamer sequences could be encoded in the locks to recognize two inputs. Both locks needed to be opened simultaneously to activate the robot. The robot remained inactive when only one of the two locks was opened. The lock mechanism is thus equivalent to a logical AND gate, with possible inputs of cell surface antigens not binding or binding (0 or 1, respectively) to aptamer locks, and possible outputs of remaining closed or a conformational rearrangement to expose the payload (0 or 1, respectively) (Fig. 2B).

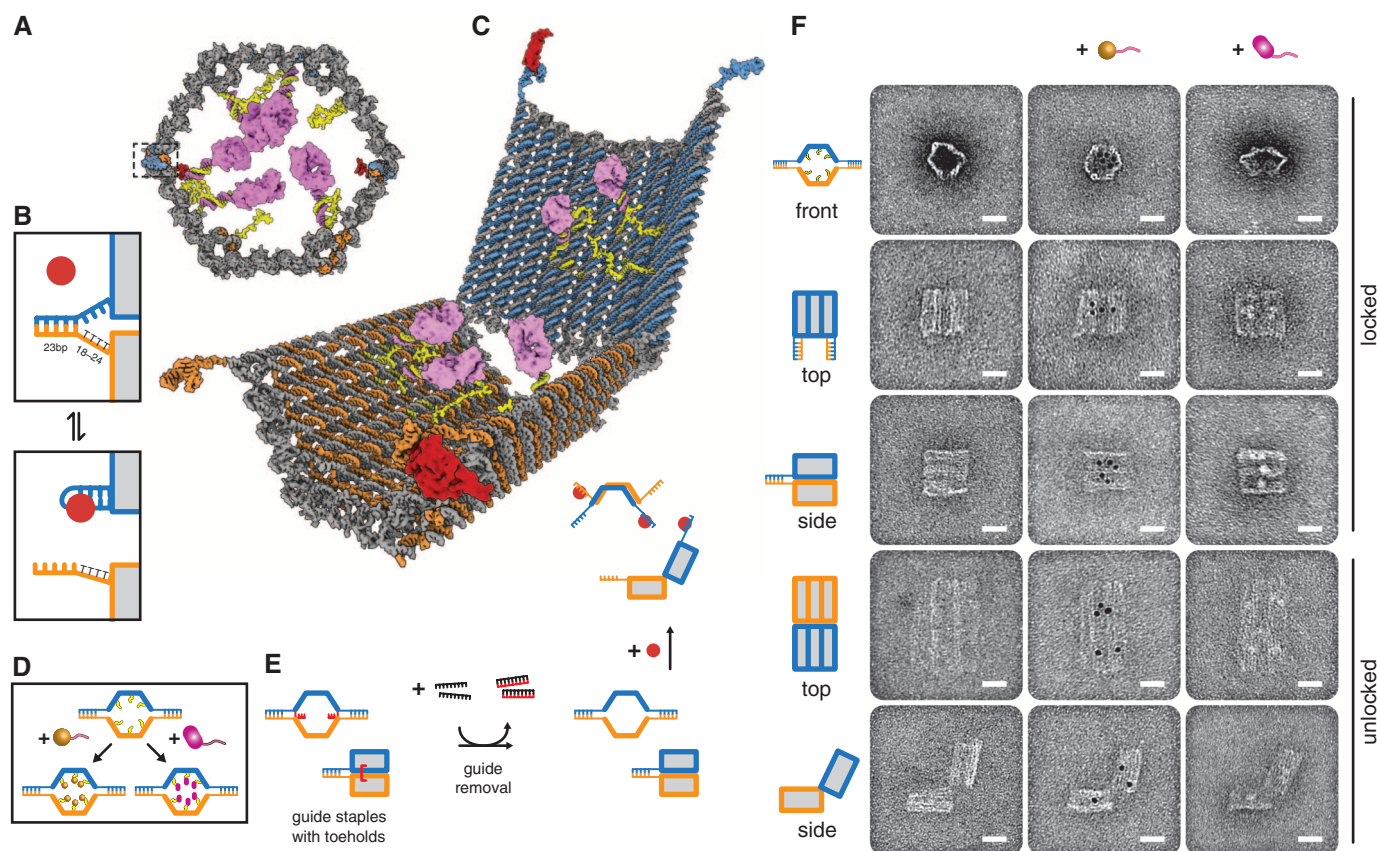


**Fig. 1.** Design and TEM analysis of aptamer-gated DNA nanorobot. (A) Schematic front orthographic view of closed nanorobot loaded with a protein payload. Two DNA-aptamer locks fasten the front of the device on the left (boxed) and right. (B) Aptamer lock mechanism, consisting of a DNA aptamer (blue) and a partially complementary strand (orange). The lock can be stabilized in a dissociated state by its antigen key (red). Unless otherwise noted, the lock duplex length is 24 bp, with an 18- to 24-base thymine spacer in the nonaptamer strand. (C) Perspective view of nanorobot opened by protein displacement of aptamer locks. The two domains (blue and orange) are constrained in the rear by

scaffold hinges. (D) Payloads such as gold nanoparticles (gold) and antibody Fab' fragments (magenta) can be loaded inside the nanorobot. (E) Front and side views show guide staples (red) bearing 8-base toeholds aid assembly of nanorobot to 97.5% yield in closed state as assessed by manual counting. After folding, guide staples are removed by addition of fully complementary oligos (black). Nanorobots can be subsequently activated by interaction with antigen keys (red). (F) TEM images of robots in closed and open conformations. Left column, unloaded; center column, robots loaded with 5-nm gold nanoparticles; right column, robots loaded with Fab' fragments. Scale bars, 20 nm.

To test the generality and robustness of the aptamer-encoded logic gating, we designed six different robots using pairwise combinations of aptamer locks drawn from a set of three well-characterized aptamer sequences: 41t, against platelet-derived growth factor (PDGF) (20), shown in red; TE17 (21), shown in yellow; and sgc8c (22), shown in blue (Fig. 2C). The six robot versions—plus a permanently locked negative control and a no-lock positive control—were loaded with fluorescently labeled antibody to human HLA-A/B/C Fab' and used to probe six different cell lines, each expressing different profiles of the "key" antigens recognized by the three chosen aptamers.

A Burkitt's lymphoma cell line (Ramos) activated none of the robots. An acute myeloid leukemia cell line (Kasumi-1) activated all robots. A third cell line, isolated from a patient with large granular lymphocytic leukemia, aggressive NK type (NKL) (23), activated robots with two 41t locks, two TE17 locks, and with one 41t and one TE17 lock. The baseline negative signal for NKL cells was higher than other cell lines because of NKL background fluorescence. A fourth cell line, isolated from acute T cell leukemia (Jurkat), activated robots bearing two TE17 locks, two sgc8c locks, as well as one TE17 lock and one sgc8c lock. The fifth line was isolated from acute lymphoblastic

leukemia (CCRF-CEM) and had a similar profile to Jurkat cells. Finally, a neuroblastoma cell line (SH-SY5Y) activated robots with two sgc8c locks. The lower intensity of the positive signals in the neuroblastoma cell line may be caused by the lower level of surface HLA-A/B/C expressed on these cells, and fluorescence intensities may be affected in general by expression levels of both aptamer keys and antibody payload targets.

We further examined the performance of the logic-gating mechanism in three ways. First, we tested the ability of the robot to selectively bind to a single cell type (NKL<sup>PTK7+/+</sup>) in a mixed population of two cell types (NKL<sup>PTK7+/+</sup> and Ramos).

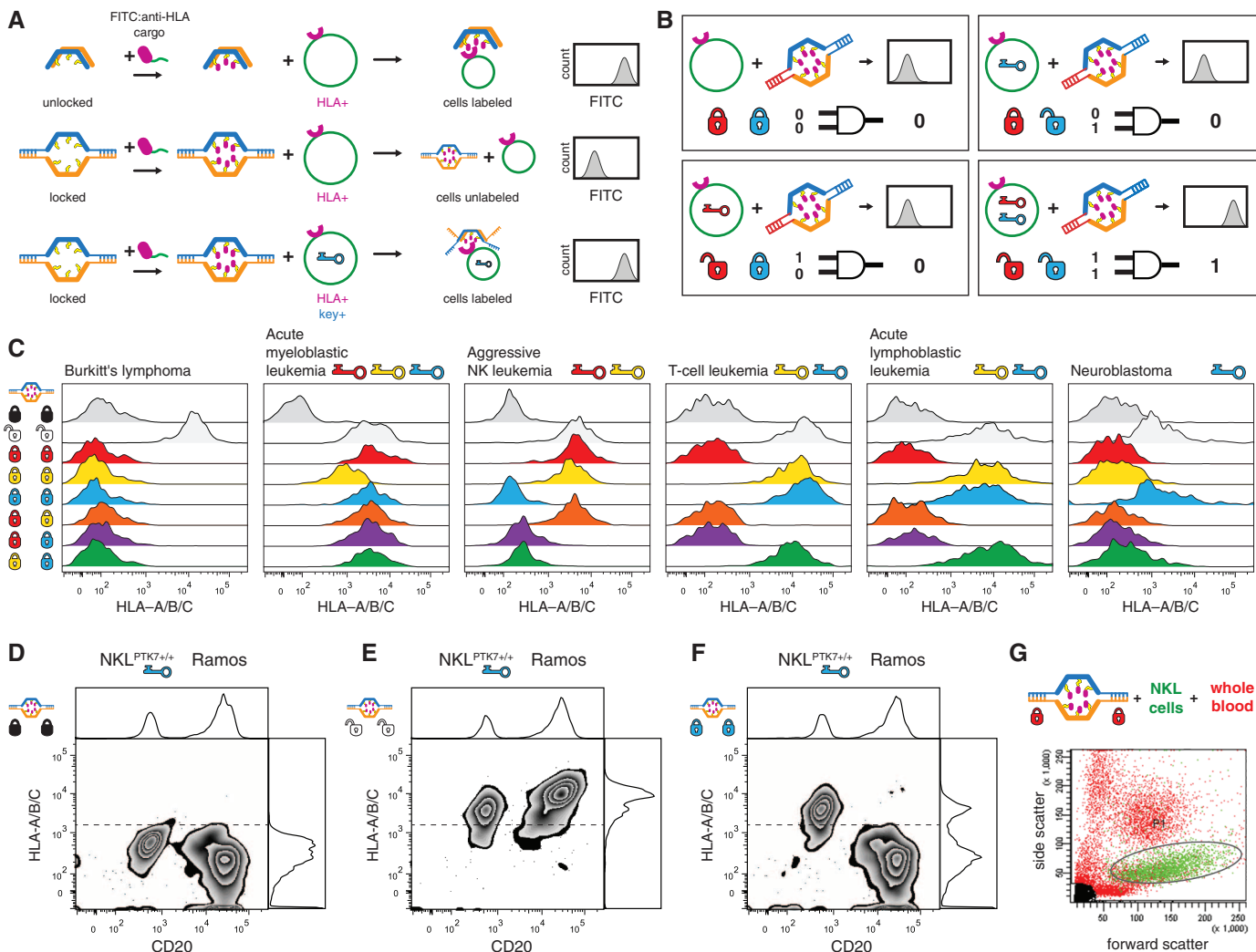


**Fig. 2.** Analysis of logic-gated nanorobot activation by different cell types. **(A)** Experimental scheme. Nanorobots were loaded with fluorescently labeled antibody Fab' fragments to human HLA-A/B/C. In their unlocked state, nanorobots will bind to any cell expressing the HLA-A/B/C antigen (top). They remain inactive in the presence of key<sup>-</sup> cells (middle) but activate upon engaging key<sup>+</sup> cells (bottom). **(B)** Truth table for nanorobot activation. The aptamer-encoded locks function as an AND gate responding to molecular inputs (keys) expressed by cells. Color match indicates lock-and-key match. Aptamer-antigen activation state serves as input; output is manifested as nanorobot conformation. **(C)** Eight different nanorobot versions (10 to 100 fmol, loaded with anti-HLA-A/B/C antibody fragments at a molar excess of 20) were tested with six different cell types expressing various combinations of antigen keys by incubating for 5 hours. Each

histogram displays the count of cells versus fluorescence due to anti-HLA-A/B/C labeling. **(D)** NKL cells (50,000 per sample, with transiently induced expression of PTK7 (NKL<sup>PTK7+/+</sup>), Ramos cells (100,000 per sample), fluorescein isothiocyanate (FITC)-labeled antibody to human CD20 (0.1 μg/ml), and permanently locked robots loaded with allophycocyanin-labeled antibody to human HLA-A/B/C Fab' were incubated at room temperature for 5 hours. No labeling is observed, as locked robots remain inactive. **(E)** Unlocked robots react with both cell populations. **(F)** sgc8c-gated robots react only with the cell population expressing the PTK7 key. **(G)** Forward- versus side-scatter dot plot of 4:1 mixture of healthy human whole-blood leukocytes and NKL cells. Nanorobots loaded with anti-CD33 Fab' payload and gated with 41t locks selectively label NKL cells. Off-target binding occurred in 0.6% of sampled cells.

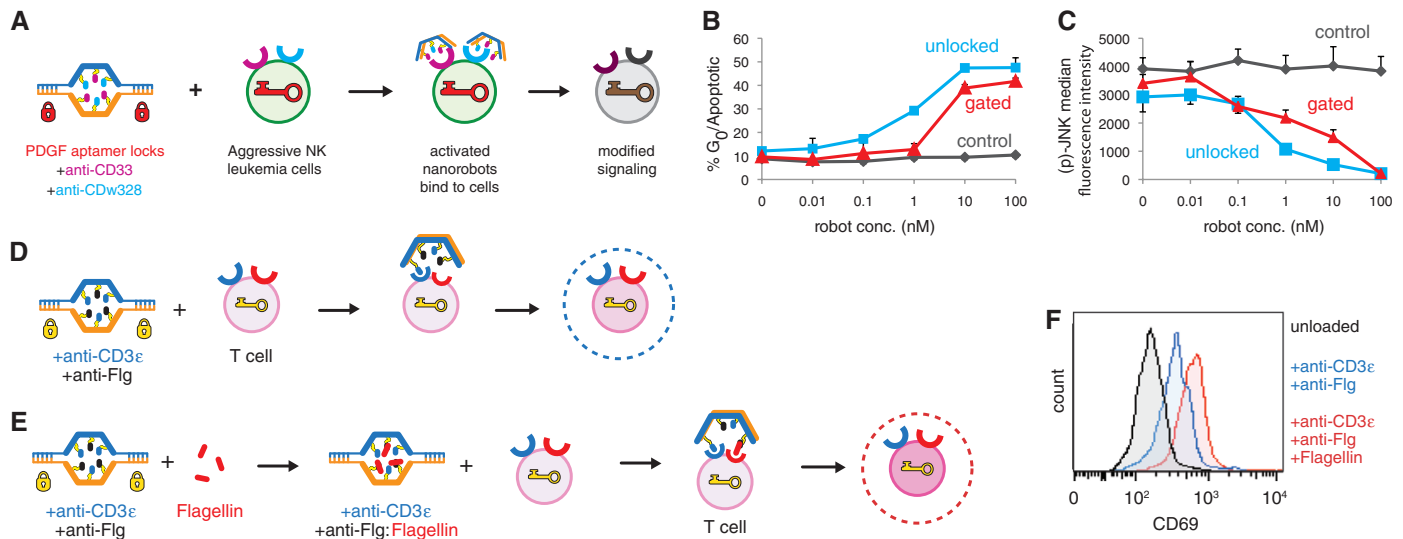


**Fig. 3.** Nanorobots manipulate target cell signaling. **(A)** Experimental scheme. A single dose of nanorobots loaded with an equal mixture of antibody to human CD33 and antibody to human CDw328/Siglec-7 Fab' fragments (cyan and magenta, respectively, each at a molar excess of 10 over nanorobots) and gated by 41t locks recognizing platelet-derived growth factor (PDGF) were used to treat NKL cells at various concentrations (0 to 100 nM). Phosphorylation of JNK was measured after 72 hours by intracellular flow cytometry. **(B)** NKL cells (10,000 per sample) treated with nanorobots were analyzed after 72 hours for cell cycle distribution by propidium

iodide (5 μg/ml). **(C)** Phosphorylation level of JNK as a function of robot concentration (lowest, 0; highest, 100 nM) after 72 hours. Error bars for (B) and (C) represent SEM of two biological replicates. **(D)** and **(E)** Incremental activation of T cells by nanorobots loaded with antibody to human CD3ε (blue) and antibody to flagellin Fab' (black). Nanorobots (50 nM) with **(E)** and without **(D)** pre-incubation with flagellin (red; 100 pg/ml) were reacted with Jurkat T cells (pink) for 1 hour at 37°C. **(F)** Histograms showing T cell activation after nanorobot treatment, as measured by labeling with FITC-labeled antibody to CD69.

Three versions of the robot were tested: a permanently closed version in which the guide staples were not removed, an open version in which no guide staples or aptamer locks were included, and a gated version using two sgc8c locks, which we expected to target only the PTK7-expressing NKL cells (Fig. 2, D to F, and figs. S22 and S23). The gated version discriminated between the two cell types, only binding to NKL cells. Second, to further simulate physiological conditions, we mixed NKL cells with healthy whole-blood leukocytes and found that robots gated with 41t locks discriminated those NKL cells with high precision (Fig. 2G and fig. S19). Third, we examined the sensitivity of the nanorobots to cell concentration using a background of 1e6 Ramos cells, tested for the ability of an sgc8c-gated robot to bind to Jurkat<sup>PTK7+/+</sup> cells. Nanorobots were activated for every cell count, from 1e6 cells down to the single-cell level (fig. S24).

Finally, we investigated the ability of an activated robot to interface with cells and stimulate their signaling in separate inhibition and activation tasks. We first chose to target NKL cells using a pair of 41t locks, and loaded the robots with a combination of antibody to human CD33 and antibody to human CDw328 Fab' fragments, which have been shown to induce growth arrest in leukemic cells (24). The robots induced growth arrest in NKL cells in a dose-dependent fashion (Fig. 3, A and B). The robots suppressed Jun N-terminal kinase (JNK) (Fig. 3C) and Akt (protein kinase B) signaling in this process (fig. S27). We then used T cells to test various methods of

signaling pathway activation (Fig. 3, D to F). Robots loaded with combinations of antibody to human CD3ε Fab' and antibody to flagellin Fab' were mixed with T cells and found to induce activation (Fig. 3, D and F). Previous work has shown that flagellin can augment T cell activation (25). We found that our nanorobots were able to collect flagellin from a 100 pg/ml solution and induce augmented T cell activation (Fig. 3, E and F). These findings demonstrate that the robots can induce a variety of tunable changes in cell behavior. Furthermore, biologically active payloads may be bound indirectly via interactions with antibody fragments, enabling applications in which the robot carries out a scavenging task before targeted payload delivery.

**References and Notes**

1. P. W. K. Rothmund, *Nature* **440**, 297 (2006).
2. Y. Ke *et al.*, *Nano Lett.* **9**, 2445 (2009).
3. S. M. Douglas *et al.*, *Nature* **459**, 414 (2009).
4. H. Dietz, S. M. Douglas, W. M. Shih, *Science* **325**, 725 (2009).
5. A. Kuzuya *et al.*, *ChemBioChem* **10**, 1811 (2009).
6. N. V. Voigt *et al.*, *Nat. Nanotechnol.* **5**, 200 (2010).
7. N. Stephanopoulos *et al.*, *Nano Lett.* **10**, 2714 (2010).
8. M. N. Stojanovic, D. Stefanovic, *Nat. Biotechnol.* **21**, 1069 (2003).
9. G. Seelig, D. Soloveichik, D. Y. Zhang, E. Winfree, *Science* **314**, 1585 (2006).
10. Y. Benenson, B. Gil, U. Ben-Dor, R. Adar, E. Shapiro, *Nature* **429**, 423 (2004).
11. B. Ding, N. C. Seeman, *Science* **314**, 1583 (2006).
12. E. S. Andersen *et al.*, *Nature* **459**, 73 (2009).

13. S. M. Douglas *et al.*, *Nucleic Acids Res.* **37**, 5001 (2009).
14. See supporting material on Science Online.
15. N. Hamaguchi, A. Ellington, M. Stanton, *Anal. Biochem.* **294**, 126 (2001).
16. R. Nutiu, Y. Li, *J. Am. Chem. Soc.* **125**, 4771 (2003).
17. J. J. Boniface *et al.*, *Immunity* **9**, 459 (1998).
18. A. P. Alivisatos *et al.*, *Nature* **382**, 609 (1996).
19. B. Yurke, A. J. Turberfield, A. P. Mills Jr., F. C. Simmel, J. L. Neumann, *Nature* **406**, 605 (2000).
20. L. S. Green *et al.*, *Biochemistry* **35**, 14413 (1996).
21. Z. Tang *et al.*, *Anal. Chem.* **79**, 4900 (2007).
22. Y. F. Huang *et al.*, *ChemBioChem* **10**, 862 (2009).
23. M. J. Robertson *et al.*, *Exp. Hematol.* **24**, 406 (1996).
24. C. Vitale *et al.*, *Proc. Natl. Acad. Sci. U.S.A.* **98**, 5764 (2001).
25. Z. Ye, C. M. L. Lee, G. W. Sun, Y. H. Gan, *Infect. Immun.* **76**, 2541 (2008).

**Acknowledgments:** We thank J. Ritz for providing NKL cells; C. Reynolds for technical assistance with NKL cells; C. Strong and G. McGill for assistance with 3D visualization using Molecular Maya; A. Marblestone for helpful discussions; and J. Markson for comments on the manuscript. S.M.D. holds a Career Award at the Scientific Interface from the Burroughs Wellcome Fund and a Wyss Technology Development Fellowship, and I.B. is supported by a fellowship from the Life Sciences Research Foundation. S.M.D. and I.B. designed and performed the experiments and analyzed the data; S.M.D., I.B., and G.M.C. wrote the manuscript.

**Supporting Online Material**

www.sciencemag.org/cgi/content/full/335/6070/831/DC1  
 Materials and Methods  
 SOM Text  
 Figs. S1 to S27  
 Table S1

16 September 2011; accepted 12 January 2012  
 10.1126/science.1214081